Nonlinear X waves in second-harmonic generation: Experimental results

O. Jedrkiewicz,[1] J. Trull,[1,*] G. Valiulis,[2] A. Piskarskas,[2] C. Conti,[3] S. Trillo,[3,4] and P. Di Trapani[1]
[1]*INFM and Department of Chemical, Physical and Mathematical Sciences, University of Insubria, Via Valleggio 11, 22100 Como, Italy*
[2]*Department of Quantum Electronics, Vilnius University, Sauletekio Avenue 9, building 3, LT-2040 Vilnius, Lithuania*
[3]*Istituto Nazionale di Fisica della Materia (INFM)-RM3, Via della Vasca Navale 84, 00146 Roma, Italy*
[4]*Department of Engineering, University of Ferrara, Via Saragat 1, 44100 Ferrara, Italy*
(Received 8 April 2003; published 22 August 2003)

X waves, spatiotemporal generalization of the monochromatic Bessel- (or Durnin-) type beams, are known in linear acoustic, microwave and optics for their unique property of defeating both spatial and temporal spreadings. Recently, we brought to the attention that X-type waves are also the key to understand the spatiotemporal dynamics observed in the nonlinear (high intensity) regime. Indeed, X waves represent the normal-propagation mode for a wide class of parametric interactions described by hyperbolic nonlinear models featuring spatial self-focusing and temporal self-broadening. Here, we provide a complete and detailed description of the experiment in which the spontaneous appearance of X waves has been observed. The experiment concerns frequency doubling of a 170-fs, 50-μm standard laser wave packet in a 22-mm lithium triborate crystal, tuned for second-harmonic generation with positive phase mismatch, positive group-velocity dispersion, and large group-velocity mismatch. Conventional beam-profile and autocorrelation measurements at the crystal output face show evidence of spatiotemporal self-trapping. The characterization of the free-space propagation reveals sub-Gaussian diffraction and pulse broadening, consistent with the presence of angular dispersion. Space-resolved autocorrelations indicate the generation of an X-type profile.

DOI: 10.1103/PhysRevE.68.026610 PACS number(s): 42.65.Tg, 42.65.Jx, 42.65.Re

I. INTRODUCTION

The progress in understanding and controlling the ultrafast nonlinear dynamics of optical waves has gone through a number of milestones in quantum electronics and its applications [1–4]. Spatial self-focusing [5–7], whose evidence in laser-rod filamentation dates back to the first developments of nonlinear optics, is currently used for the Kerr-lens mode locking in modern femtosecond (fs) laser technology. Its temporal analog, the self-phase modulation, is the key element engaged to achieve pulse compression down to few optical cycles as well as to produce temporal solitons in fibers [8], giving new impetus to the field of long-distance, high-speed, optical communications. It is the nonlinear coupling between modes with different temporal frequencies (as in continuum generation [9–11], $\chi^{(2)}$ parametric interaction or high-order harmonic generation in gas) which provides coherent fs sources ranging from the mid infrared to the soft x rays. Temporal and spatial nonlinear dynamics are also considered in detail in quantum optics for their application to squeezing, to low-noise image amplification, and to other important effects related to the generation of quantum entangled states of light [12].

As a matter of fact most of the description, modeling and characterization of the processes mentioned above has paid attention either to the pure spatial or to the pure temporal domain. Recently, thanks to the easier access to fast computers for three-dimensional (3D) calculations and to ultrafast laser facilities and diagnostic for the experiments, nonlinear optics is paying more and more attention to those regimes characterized simultaneously by ultrashort pulses and by strongly focused beams. The applications vary from the integrated microphotonics and nanophotonics to the nonlinear ultrafast spectroscopy ''in imaging,'' from the utilization of ultra-short pulses for the treatment of animal or vegetable tissues to the development of coherent sources in the x-ray–visible–ultraviolet range or to the generation of relativistic plasma. Several results already witness a rich phenomenology which cannot be properly captured by relying on the assumption that the temporal and spatial dynamics are disjoint [13–17]. In fact, the spatiotemporal degree of freedom given by the angular dispersion (the dependence of temporal frequencies on angles), not accounted for in any separable-like approach, leads to a wave-packet (WP) dynamics that cannot be described as the simple combination of the known spatial and temporal processes. This means, for instance, that the use of cw Gaussian WPs, successfully adopted for the description of laser radiation and linear or nonlinear propagation in the presence of diffraction, has to be reconsidered once the real 3D dynamics is taken into account.

In this scenario, the ''hunt for light bullets'' [18,19] and for linear localized spatiotemporal WPs address one of the most fascinating features of light propagation, providing a road map for understanding the features of space-time interplay. Besides this fundamental aspect, ideal particlelike behaviors of WPs are important in several applications, also outside the field of optics. Examples are microscopy, tomography, laser-induced acceleration of particles, ultrasound medical diagnostics, Bose-Einstein condensation, volume optical-data storage, optical interconnects, and long-distance communications. However, to date, linear and nonlinear optics have followed different strategies to achieve space-time localization, as illustrated in detail below. The discovery of

*Also at Dept. Fisica i Enginyeria Nuclear, UPC Terrassa, Spain.

nonlinear X waves has finally combined them [20].

In linear physics, the search for WPs that are both stationary (i.e., invariant upon propagation) and sufficiently localized (both in the transverse and in the longitudinal, or temporal, coordinate) has brought to the prediction of a number of modes, called splash modes, focus-wave modes, slingshot pulses, nondiffracting X waves, Bessel-X pulses, etc. (see, e.g., Refs. [21–34] and references therein) which can be considered as spatiotemporal generalization of the monochromatic, nondiffracting, Bessel- (or Durnin-) type beams [35]. Experimentally, localized wave transmission has been tested in acoustics [36,37], optics [38–40], terahertz waves [41], and microwave antennas [42] (the latter with emphasis on superluminal features of the localized WP [43]). In this case, the localization is achieved by means of dispersion management, i.e., the idea that intrinsic (e.g., chromatic) material dispersion can be counterbalanced by the effect of the WP angular dispersion. This idea can be easily understood by considering the one-dimensional case of the so-called ''tilted pulses.'' These are WPs with amplitude front tilted with respect to the phase one. They are generated when a linear (e.g., in one plane) angular-dispersive element, such as a diffraction grating or a prism, is used in conjunction with conventional ultrashort pulses. The angular spreading of the monochromatic plane-wave components at different frequencies affects their longitudinal wave numbers (along a given direction) leading to an ''effective'' dispersion associated with the WP. Such an angular control of chromatic dispersion has been first introduced for compensating the group-velocity difference between the harmonic WPs in second-harmonic generation (SHG) [44,45], either in presence of material angular dispersion (i.e., lateral walk-off) or in the presence of a noncollinear interaction scheme. Regarding higher-order effects, it has also been predicted [46], and experimentally demonstrated [47], that tilted pulses allow for the control of the effective group velocity dispersion (GVD) [48,49], and thus for the achievement of dispersion-free propagation of fs pulses in media with large, positive (normal) GVD. Note that tilted pulses are necessarily not localized in space since they extend in the plane of the angular dispersion. The achievement of stationarity and localization in both temporal and spatial coordinates is obtained by combining the angular dispersion due to the tilt and the conical shape characteristic of Bessel beams. Thus, the resulting WP can be equivalently described either as a superposition of Bessel beams with angular dispersion (as usually done in the literature) or, equivalently, as a superposition of tilted pulses with carrier k vector distributed over a cone (i.e., ''revolving'' tilted pulse) [50]. The resulting stationary intensity distribution has an X-shaped profile on any plane which contains the propagation axis, with a central peak sustained by slow-decaying tails. The study of the angular dispersion of the general linear eigenmode indicates that X waves are well representative of the entire class of all possible stationary and localized WPs. Importantly, in the general case of bell-shaped spatially and temporally narrow spectra (centered around carrier frequencies), X waves require normal material GVD [51,52].

In nonlinear optics of bulk media, in order to obtain a true stationary WP sustained by a fast nonlinearity, one needs 3D spatiotemporal localization (1+3D solitons) [18]. In fact, any localized mode in a subdimensional space is expected to be ultimately not stationary due to noise-driven modulational instability (MI) in the additional dimension(s). Relying upon the few indications available from recent experiments in $\chi^{(2)}$ media [53], one would actually conclude that such a MI impact is rather strong in practical settings, leading to a typical 3D dynamics no matter whether large beams of long pulses are used. The 1+1D temporal [15] and 1+2D spatiotemporal $\chi^{(2)}$ solitons [54] obtained by the use of extended tilted pulses exhibit spatial filamentation just above threshold [55]. Direct evidence of the temporal breakup of the $\chi^{(2)}$ spatial solitons has not been reported yet, but the counterintuitive observation of spatial solitons with apparent lacking of the high-frequency (pump) mode [56] has been attributed to noise-seeded spatiotemporal instability effect [52,57], occurring in normally dispersive crystals. The basic idea for achieving nonspreading WPs is that the nonlinear wave front curvature can balance simultaneously the curvature due to diffraction and GVD, combining features of spatial [7] and temporal [8] solitons to form a bell-shaped localized WP, the so-called light bullet [19]. This approach requires a focusing-type (saturable for stability constraints) nonlinearity to compensate for diffraction in bulk. Importantly, in sharp contrast with the linear X waves, it also requires the same sign for the phase curvature induced by diffraction and dispersion, respectively, which means anomalous material GVD. Unfortunately, the successful observation of light bullets has been hampered by several factors among which the dominant absorption of the low-frequency wave and large group-velocity mismatch (GVM) in $\chi^{(2)}$ mixing, and losses induced by the saturation mechanism in Kerr materials [58].

Recently, we have shown that the drawbacks of both the linear (which requires nontrivial input beam shaping)and the nonlinear (the elusive character of light bullets) approaches described above can be overcome by the observation that space-time localization occurs, through a focusing nonlinear material response, also in the regimes of normal GVD or dominant GVM [20,51]. In this case, trapping is accomplished by mutual balance of intrinsic, shape-induced, and nonlinear contributions in a new type of WP, namely, a nonlinear X wave. We were led to this observation while attempting to implement the radially symmetric generalization of the tilted-pulse technique employed to demonstrate $\chi^{(2)}$ temporal trapping [15]. Also in the 1D tilt case, trapping arises by mutual balance of chromatic (GVM and GVD), tilt-induced, and nonlinear temporal phase modulations. In this case, however, the absence of spatial localization prevents the balance of nonlinear spatial phase curvature, leading to the occurrence of spatial MI [55]. On the contrary X waves, having temporal features similar to the tilted pulses and being spatially localized, were expected to be stationary with respect to temporal and spatial effects. It is worth pointing out that in attempting the experiment, we started by investigating a way of generating by linear means the correct X shape of the input WP, capable of supporting the mutual balance of the three contributions mentioned above. This approach, however, has not proven successful since the construction of stationary X waves with fs pulses is known to be

a tough problem even in the linear case [28,37,59]. Nevertheless, our experiment has unexpectedly revealed a remarkable spatiotemporal mode locking process that, starting from a conventional Gaussian-type laser WP, performs spontaneously the reshaping into a localized X-shaped WP. We believe that this is the first genuine nonlinear trapping in full-dimensional (3D) physical space. In this paper, we provide a complete and detailed characterization of the measurements performed to give the evidence of this reshaping, interpreted as the spontaneous appearance of X waves occurring via mismatched SHG.

For other nonexperimental issues related to this phenomenon, we refer the reader elsewhere. For instance, the numerical simulation of the 1+3D propagation allows us to monitor the WP transformation (transient dynamics) and to investigate the quasistationary (final) stage of nonlinear propagation, against the launching conditions. The main results can be found in Ref. [51], while a detailed review on the numerical work addressing the evolution to the X wave from the input WP is currently in preparation [60]. On the other hand, the linear stability study of the continuous and plane-wave eigensolutions of the SHG model has permitted us to understand the key elements featuring the early stages of this transient characterized by colored conical emission, which trigger the X-wave formation [61]. We mention that a similar mechanism has been shown to hold in parametric amplification as well [57]. Furthermore, the discovery of X-wave solitons (nonlinear X-shaped eigenmodes of the 1+3D SHG model [62]) supports the idea that a strictly stationary regime would be ideally accessible if infinite energy is launched into the nonlinear crystal. The conical tails of these nonlinear X waves reflect the symmetry of linear dispersion relationship [51].

The paper is structured as follows. Section II is devoted to the description of the experiments: the spatial measurements are presented in Sec. II A. In Secs. II B, II C, and II D, we describe the temporal measurements carried out by means of single-shot crosscorrelation, noncollinear autocorrelation, and multiple-shots autocorrelation, respectively. A comprehensive summary of the results is given in Sec. III together with the conclusions.

II. THE EXPERIMENTAL RESULTS

The aim of the experiment was to capture the spontaneous appearance of X waves and the occurrence of quasistationary propagation mode in optical SHG performed in a quadratic nonlinear crystal of Lithium Triborate (LBO) which exhibits positive (normal) GVD [$k''(\omega)=0.016$ ps^2/m, $k''(2\omega)=0.089$ ps^2/m] and large GVM (45 ps/m). A 10-Hz Nd:Glass picosecond laser at 1055 nm was used to generate, through a second-harmonic nonlinear compressor, 170 fs pulses which in turn were used to pump a traveling-wave optical parametric generator (TOPAS, Light Conversion Ltd). The latter was tuned to obtain nearly transform limited 170 fs pulses at 1060 nm. These were launched for the X-wave generation inside the nonlinear crystal (a 22-mm sample of LBO) cut for noncritical type I phase matching to avoid spatial walk off. Note that the value of GVM is such that, in the linear regime, a 170 fs infrared pulse would split from its second-harmonic (SH) pulse within about 1/5 of the crystal length. By changing the crystal temperature T, the collinear phase mismatch between the interacting waves $\Delta k = 2k_\omega - k_{2\omega}$ could be varied. For crystal temperatures higher than the phase-matching temperature of 154 °C, Δk is positive. This regime is known to support spatial solitary waves with dominant energy content at fundamental frequency (FF) and to sustain preferential noncollinear interaction [53] (with the SH on axis and the FF over a cone), being $|k_{2\omega}| < |2k_\omega|$. On the contrary, for temperatures below the phase-matching one, FF self-defocusing should occur [53,63]. All the measurements related to the nonlinear X-wave characterization have been carried out at $T=180$ °C corresponding to $\Delta k = 30\ \mathrm{cm}^{-1}$. Note that for our input pulse duration, this value approximately corresponds to the boundary of the stationary limit of the cascade process, which determines the possibility of at least two cycles of frequency conversion occurring before the pulses can move away from each other because of GVM [64]. Several experimental settings and diagnostic setup were mounted to characterize the WPs at FF and SH at the output of the nonlinear crystal and beyond (during propagation in air). All spatial and temporal measurements were performed with input pump energy ϵ_p in the 0–1 μJ range.

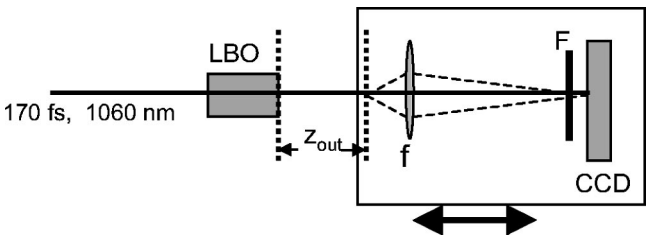

FIG. 1. Experimental apparatus scheme for near- and intermediate-field spatial measurements.

A. Spatial measurements

This section describes the characterization of the spatial intensity distribution of WPs exiting the LBO crystal, for both the FF and the SH waves. The profiles were measured in the near field (i.e., at the crystal output face), in the intermediate field (i.e., by following the free-space propagation for a few centimeters outside the crystal), and in the far field. The main results are (i) the generation of self-trapped beams into the crystal; (ii) the occurrence of sub-Gaussian (Gaussian) diffraction for the WPs at FF (SH) in free-space propagation; and (iii) the appearance of a Bessel-like contribution to the FF angular spectrum and the presence of relevant angular dispersion in both waves.

The setup for the near- and intermediate-field measurements is schematized in Fig. 1. The FF input pulse was focused at the crystal input face, down to a 65-μm FWHM beam waist, by adjusting the position of the focusing lens (not shown) placed in front of the LBO. The use of a $\lambda/2$ plate and a polarizer (not shown in the figure) allowed for a careful adjustment of the input pump energy ϵ_p. The single lens placed on the beam path after the nonlinear crystal im-

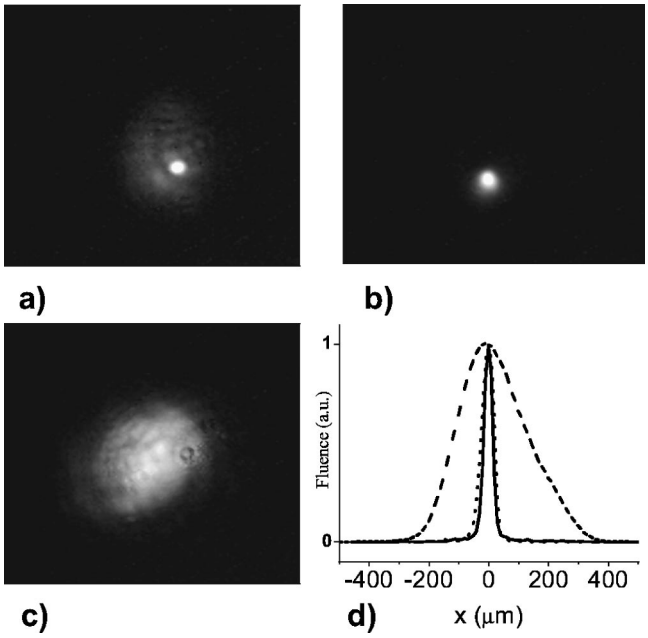

FIG. 2. Near-field spatial patterns at the output face of the LBO crystal. (a) FF and (b) SH output beams in nonlinear regime ($\epsilon_p = 0.6\ \mu$J). (c) FF output beam in linear regime ($\epsilon_p = 0.2\ \mu$J). (d) Corresponding beam profiles: the continuous and dotted curves refer to the FF and SH output beams shown in (a) and (b), respectively, whereas the dashed curve stands for FF linear (c) case. All curves are normalized to arbitrary units.

ages (with suitable magnification) the WP intensity transverse pattern from an object plane at a distance Z_{out} from the crystal, onto the 8-bit (charged coupled device) CCD-camera (Pulnix, TM-6CN) plane, which allows us to record the time-integrated beam profiles. Neutral density and color filters (F) were used to attenuate the signal and to select the desired WP (either the FF or the SH one). The readjustment of the lens position allowed for compensation of the change in optical path due to the filter replacement and to the lens chromatic aberration. The entire diagnostics was mounted on a translation stage that allowed to perform measurements at $Z_{out}=0$ (near field) and a scan in the range $Z_{out}=0-10$ cm (intermediate field). The far-field measurements were performed by moving the CCD in the f-lens focal plane. Frequency resolved angular spectra were acquired by means of a CCD based spectrograph (not shown in the figure) with the entrance slit placed in the f focal plane.

The near-field measurements showed that, for crystal temperature tuned at 180 °C ($\Delta k = 30\ \text{cm}^{-1}$) and for ϵ_p exceeding the threshold value of 0.25 μJ, spatial beam narrowing occurs for both the FF and the SH waves. Figure 2 shows typical snapshots for the FF (a) and the SH (b) fluence distributions above threshold and also in linear regime (c) for the FF wave. The corresponding profiles measured along a beam diameter are presented in Fig. 2(d). Mutually trapped FF and SH beams characterized by a FWHM diameter of about 30 μm and 45 μm, respectively, could be clearly observed. Since these figures indicate a diffraction-free propagation of the FF input WP over two diffraction lengths, the beam exhibits spatial solitonlike features [53,65]. We mention here that this feature was confirmed by the results relative to a 45-μm input beam (this beam size was used, too, as illustrated in the temporal measurements section), where similar diffraction-free propagation occurs. With the chosen value of the collinear phase mismatch between the FF and SH waves, the effects of GVM are not too deleterious if we consider a 170 fs pulse duration, and the spatial trapping process being marginally within the acceptance angle can be understood [64]. Nevertheless, since, as we shall see in Sec. II D, we observe in the same energy range strong FF pulse compression (measuring a pulse duration of 20 fs, at the crystal output), the effects of GVM (and GVD) are in fact much stronger and therefore the trapping mechanism turns out to be extremely remarkable and quite unexpected. Note also that the FWHM diameter is larger for the SH (as compared with the FF beam), in contrast with the standard $\chi^{(2)}$ spatial soliton regime [7,53]. Keep on increasing the energy far above threshold, typically for $\epsilon_p \geqslant 0.8\ \mu$J, the beams became very unstable and inhomogeneous with clear presence of continuum radiation, due to the contributions of $\chi^{(3)}$ and higher-order nonlinear effects. Finally, if the crystal temperature was reduced to the phase-matching value 154 °C ($\Delta k = 0$) or to 126 °C ($\Delta k = -30\ \text{cm}^{-1}$), no trapping takes place in the entire energy range. This result indicates the importance of the initial FF self-focusing in triggering the dynamics.

The results of the intermediate-field measurements are summarized in Fig. 3, which describes the beam-profile evolution during free-space propagation in the range $Z_{out} = 0-10$ cm. The normalized beam profiles of the FF and SH waves are plotted in Fig. 3(a). The corresponding full width at half maximum (FWHM) diameters are plotted in Fig. 3(b), together with the calculated values (assuming FF and SH Gaussian beams), with same FWHM diameters at $Z_{out}=0$. The results show a divergence (or a diffraction) for the FF wave 3–4 times smaller than for the Gaussian case, in good agreement with the predictions of our numerical experiments [20,60]. In contrast, the SH behaves similar to a conventional Gaussian beam.

Finally, the FF and SH radiation far-field patterns were analyzed and recorded as a function of the pump energy. Two cases (for energy just above and far above threshold) are illustrated in Fig. 4, whereas Fig. 5 displays a typical far-field angular spectra above threshold. It is worth noting, in contrast to the case of SH beam, the Bessel-like structure of the FF beam evidenced in the far-field measurements, clearly displayed in Figs. 4(a) and (b). On the other hand, as shown in Fig. 5, the frequency resolved angular spectra are characterized by the presence of angular dispersion. Note that, in the bottom spectrum that refers to the SH radiation, a high intensity frequency-shifted contribution peaked around 514 nm can be observed. This narrow-band component is generated by the nonlinear cascading process, due to the combined action of mismatch Δk and GVM, and corresponds to the detuned frequency value which yields collinear phase matching. In time domain, we expect therefore a long, nontrapped contribution to the SH radiation whose presence might prevent a careful evolution of the spatial features of the remaining portion of the pulse, expected to be trapped with the FF

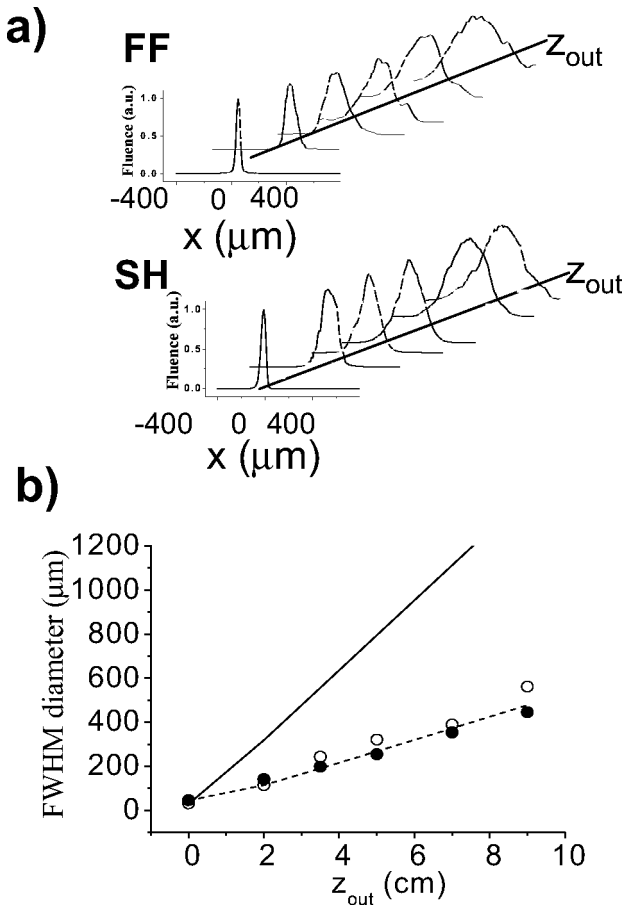

FIG. 3. (a) FF and SH transverse beam profiles at increasing distances from the crystal output face, in a nonlinear regime (all curves are normalized to the peak value of the beam profile measured at $Z_{out}=0$). (b) Evolution of the corresponding measured FWHM for the FF (open dots) and SH (full dots) beams compared with the values calculated for Gaussian beams (FF, continuous line; SH, dashed line).

one. This can explain why a virtually Gaussian behavior for the SH beam was recorded via time-integrated measurements [as shown in Fig. 5(b)], in spite of the angular dispersion evident in the frequency resolved spectrum.

B. Temporal single-shot noncollinear cross-correlation measurements

The problem of measuring the duration of an X-type WP is substantially different from that encountered in the case of a conventional Gaussian-like WP, for the following two reasons. The first is that the WP changes dramatically its duration while it propagates in free space (in air as well as in vacuum), due to its effective GVD. In order to overcome this problem, we have adopted different approaches, with different advantages and drawbacks. In this section, we describe a cross-correlation scheme that allows us to measure the WP duration as close as possible to the LBO crystal, without any intermediate optical element. In Sec. II C, we will describe an autocorrelation setup that transfers the WP field distribution from the LBO output face to the correlator plane by suitable imaging; in Sec. II D, the advantage of spatial clipping of the central portion of the WP will be discussed. The second reason is that the WP duration is not exhaustive on the temporal features of an X wave, since its temporal structure changes noticeably across the beam. In this section, the attention is focused on the central part of the WP only. In Sec. II C, the features of the WP tails will be addressed by using a high dynamic range CCD detector. In Sec. II D, the use of a variable clipping combined with photodiode detec-

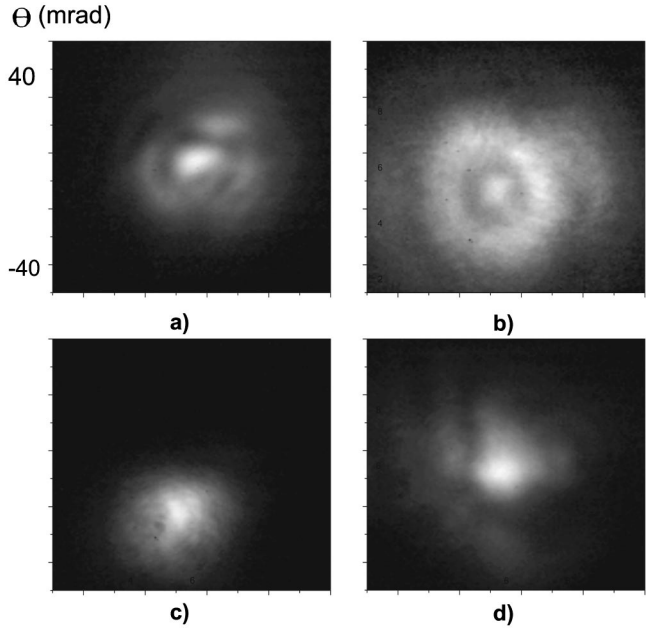

FIG. 4. Far-field transverse patterns of the FF [(a) and (b)] and SH [(c) and (d)] output radiations. The input energy is $\epsilon_p=0.3$ μJ in (a,c), and $\epsilon_p=0.7$ μJ in (b,d). The vertical and horizontal axes have the same angular scale on all pictures.

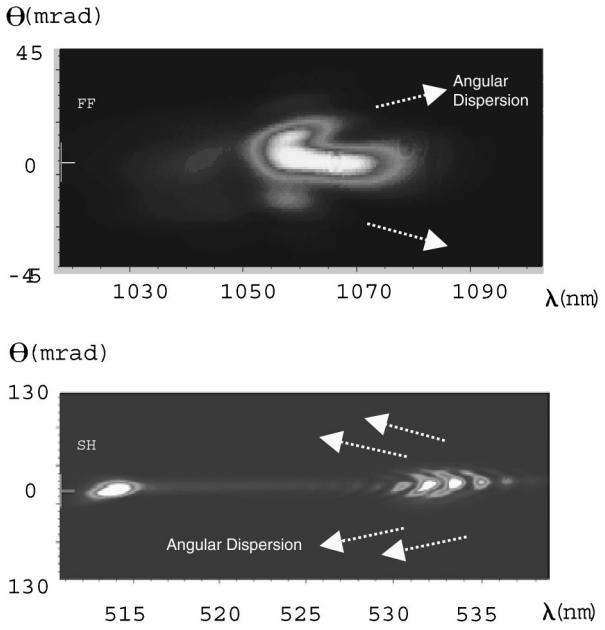

FIG. 5. Far-field spectra of the FF (top) and SH (bottom) output beams ($\epsilon_p=0.6$ μJ).

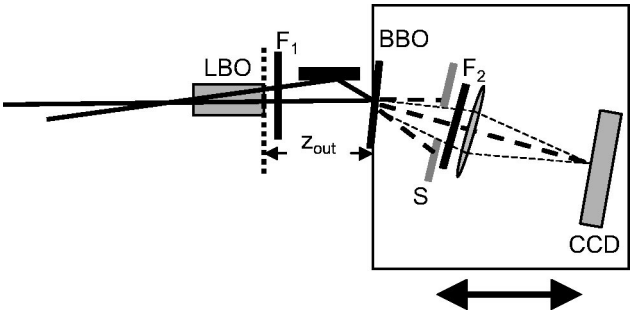

FIG. 6. Experimental setup for single-shot noncollinear cross-correlation measurements.

tion will be presented. The results of this section outline the occurrence of strong temporal compression in the LBO sample, under the same operating conditions where spatial self-focusing was observed. This feature is followed by temporal broadening during propagation in air. A slight change in the focusing conditions has been shown to have a strong impact on the temporal dynamics.

A scheme of the setup used is illustrated in Fig. 6. The solution adopted to measure the WP duration as close as possible to the LBO output face exploits cross correlation between two virtually identical WPs generated in the same LBO crystal by two replicas of the FF input pulse. This scheme avoids the relatively long path involved in standard autocorrelation schemes. The two generated WPs were then made to collide just outside the LBO for single-shot noncollinear cross correlation via frequency mixing in a thin (100-μm) β-barium borate (BBO) $\chi^{(2)}$ nonlinear crystal. The sum-frequency (SF) field generated in the BBO was then imaged on the CCD camera (Pulnix). A color filter (F_1) was used to remove the strong SH radiation generated inside the LBO. A slit (S) was mounted after the BBO crystal in order to eliminate the FF and SH contributions introduced by the second-harmonic components generated from each single FF beam, and a second color filter (F_2) was used to remove the scattered infrared radiation.

The motivation for the choice of a single-shot detection, instead of the more common scanning correlation technique, was that of facilitating the search for the optimum operating condition. This is not a trivial task if one thinks about the low repetition rate of our system (10 Hz) and the relevant shot-to-shot fluctuations caused by the large number of cascaded nonlinear processes used in the setup. Note that the choice of noncollinear interaction (besides being the natural one for minimizing the beam path) is also necessary for any single-shot correlation approach. The basic idea on which the adopted scheme operates is easily understood under the assumption that two identical WPs are delivered by the two channels and under the approximation of constant intensity and duration of the WPs over a sufficiently large beam area (for the validity of these approximations, see the discussion below). In this limit, in fact, the method proposed is identical to the usual single-shot noncollinear autocorrelation [66,67]. With this setup, the spatial-intensity distribution of the generated sum-frequency field gives, in single shot, the entire temporal intensity autocorrelation function, since different lateral portions of the beams collide with different relative delay. Here, the temporal (or delay) coordinate is the horizontal one, the two beams colliding in the horizontal plane. The autocorrelation traces sampled at different vertical coordinates might be used to extract information on the temporal structure along different portions of the beam (see Sec. II C).

Before presenting the data, however, it is important to discuss the main limitation of the setup and the approximations involved, resulting from the use of a noncollinear scheme in conjunction with X-type wave profiles. First of all, since we are not dealing with plane-wave pulses but with focused beams, special care should be taken in preventing the clipping of the correlation area by the rather small beam width. We solved this problem by taking a fairly large angle (39°) between the two beams. This option, which for conventional pulses has the only drawback of reducing the temporal resolution, here might lead to the appearance of some pedestal in the correlation trace due to the contribution of the tilted WP tails (see the discussion about Fig. 11). This problem, however, should not affect significantly the FWHM value and therefore it is not relevant for the purpose of detecting the nonlinear compression. A second drawback of our setup is related to the slightly different optical path length followed by the two WPs from the LBO to the BBO crystal. In order to guarantee the synchronization of the two WPs on the BBO, a slightly different path length was settled between the common focusing lens (not shown) and the LBO. Because of that, we unavoidably ended up with two slightly different positions (about 1–2 mm) of the beam waist in the LBO, preventing in turn the generation of two identical WPs. Again, this limitation dos not affect substantially the FWHM evaluation but might have an impact on the possibility of detecting the fine spatiotemporal WP structure, for which autocorrelation measurements are better suited (see Sec. II C).

Figure 7 shows the results obtained for an input pulse energy of 0.6 μJ and with the BBO crystal placed as close as possible (3.5 cm) to the LBO output face. Figures 7(a) and 7(b) give the measured SF intensity distributions for two different positions of the input beam waist, namely, with the waist (65 μm) at the crystal input face [Fig. 7(a), henceforth called case I] and with the waist (focused down to 45 μm) 15 mm before the crystal [Fig. 7(b), henceforth denoted as case II]. For a more quantitative description, the corresponding profiles at the beam center are reported in Fig. 7(c), where the trace relative to the linear regime is also shown for comparison. In the inset, we show the results of numerical simulations (more detail will be reported in Ref. [60]) relative to case I. The results show an evident compression in the central part of the beam, the estimated FWHM pulse duration (under the assumption of Gaussian profile) going from 170 fs, in the linear regime, down to 30 and 40 fs for cases I (central spike) and II, respectively. The results also reveal a large sensitivity of the process to the focusing conditions. In fact, the two secondary peaks appearing in the cross-correlation profile relative to case I (see Figs. 7(a) and 7(c), thick solid line) indicate the presence of a satellite, which is absent in the case-II regime (see Figs. 7(a) and 7(c), dashed-dotted line). Our simulations (data not shown) indicate that

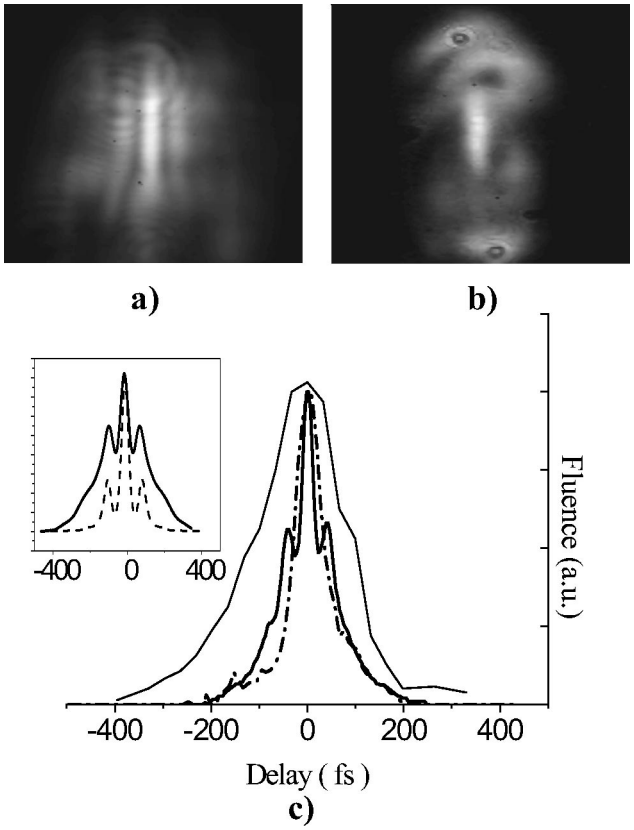

FIG. 7. Single-shot cross-correlation patterns recorded in noncollinear configuration at 3.5 cm from the output face of the LBO crystal in case I (a) and case II (b) in the nonlinear regime ($\epsilon_p = 0.6\ \mu J$). In (c) the corresponding temporal correlation traces at beam center are shown (case I, thick solid line; case II, dashed-dotted line) and compared with the linear regime (thin solid line). The inset shows the expected traces calculated from numerical simulations in case I, at $Z_{out}=0$ (dashed line) and $Z_{out}=3.5$ cm (solid line). Normalized units are adopted for the vertical axis.

this satellite is actually a pre-pulse, which appears as the residuum of pulse-splitting process, analogous to what occurs in case of Kerr media with normal GVD [14]. Noticeably, when slightly diverging beams are used (case II), the spatiotemporal compression takes place less abruptly than in case I, leading to the appearance of a single, compressed, WP (see Ref. [60] for a detailed presentation of the numerical results). By monitoring the cross correlation at different pump energies, we verified that the pulse compression occurs together with the spatial self-focusing. By changing the crystal temperature, we confirmed that compression occurs neither at phase matching nor for negative values of phase mismatch.

By shifting the detection system (see bounding box in Fig. 6) and thus increasing Z_{out}, we had easy access to the evolution of the temporal profile of the WP caused by its propagation in air. A sequence of cross-correlation traces acquired for Z_{out} (in case II) in the 3.5–10 cm range is presented in Fig. 8(a). The corresponding estimated FWHM pulse durations are reported in Fig. 8(b). The results show a dramatic pulse broadening in air, which is a clear indication that the generated WP possesses relevant angular dispersion.

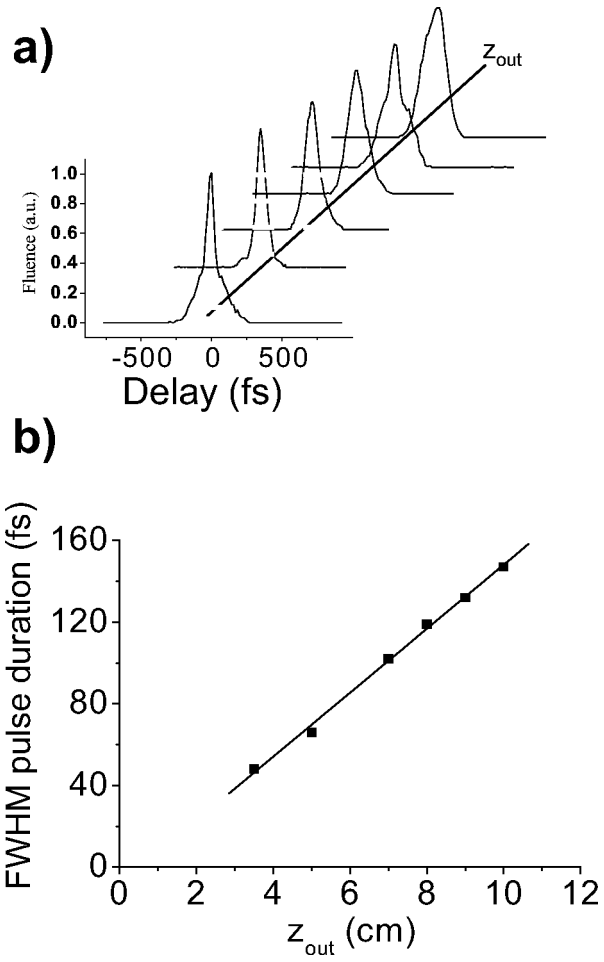

FIG. 8. Single-shot cross-correlation traces at increasing distances from the crystal output face in nonlinear regime (curves normalized to the peak value of the trace measured at $Z_{out}=0$) (a) and the corresponding estimated FWHM pulse duration (b).

C. Temporal single-shot noncollinear autocorrelation measurements

The purpose of the second correlation setup was that of recording the structure of the tails of the generated WP and thus of revealing an evidence of the X-wave formation. To this end, the measurements were performed by using a single-shot noncollinear *autocorrelation* technique which allows us to correlate two identical copies of the same WP. A higher dynamic-range, cooled, CCD camera (Andor, EEV 40-11) was used. The obtained results give a strong indication of the X-type spatiotemporal structure of the localized WP formed.

The experimental setup is illustrated in Fig. 9. Only one input beam was sent through the nonlinear LBO crystal. Two replicas of the generated FF WPs were created by means of 50/50 beam splitter and sent with an angle of 30° onto the 100-μm type I BBO crystal for noncollinear single-shot autocorrelation. In order to reconstruct the field distribution (in amplitude and phase) onto the BBO, a two-lens f-$2f$-f imaging system, conjugating an object plane close to the output face of the LBO with the BBO plane, was installed. The distance Z_{out} between the object plane and the LBO was

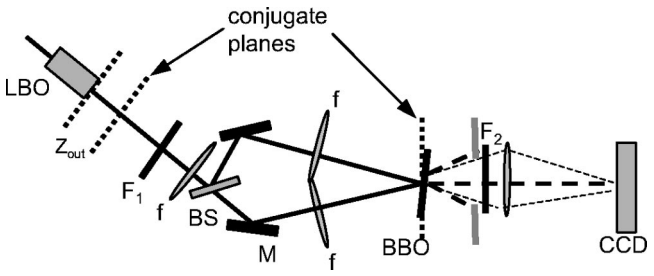

FIG. 9. Experimental setup for single-shot noncollinear autocorrelation measurements.

adjusted in such a way as to prevent the clipping of the autocorrelation by too small beam size, and to optimize for having sufficiently intense spatiotemporal tails of the WP with respect to the central part.

Figure 10 shows a typical autocorrelation image recorded in nonlinear regime in case II (in the absence of pulse satellites). A well-distinguished three-peak feature is clearly evident at the top and bottom of the autocorrelation (see white trace on top right of the figure), this being an indication of the occurrence of pulse splitting. In contrast, there is no evidence of pulse splitting at the beam center as, in fact, the autocorrelation is featured by a single peak with shoulders. These are interpreted as the effect of an overlap of the X-waves tails in the noncollinear geometry. The characteristics of the pattern shown in Fig. 10 are consistent with what was expected from mixing two X-shaped waves, as shown in Fig. 11. At the top left of this figure, the isointensity profile of an ideal X wave featured by two cones attached by their apes is shown. A section out of axis leads to two well-separated pulses (represented in gray on the picture), while a section containing the axis leads to an X-shaped profile (represented in black). The collision of the top and central sections of two X waves is schematized at the top right of the figure. In order to distinguish between the two waves, these were represented in dark and light colors, respectively. The intersection inside the BBO crystal of the top parts of the two waves is illustrated in the central part of the figure. Under the approximation of plane wave fronts, the interaction produces three well-distinguished peaks consistent with the experimental result (see the top of the autocorrelation reported on the right side). The interaction of the central parts of the two waves within the crystal is depicted at the bottom of Fig. 11. Note that the three intersection points between the two waves change their position during propagation (due to the sliding of the tails, one with respect to the other). Because of that, lateral shoulders are expected to appear consistently with the shape of the autocorrelation measured at the beam center (see the inset at the bottom right). Finally, note that because of the distance between the LBO output face and the imaging plane, because of the possible abberations of the imaging system, and because of the presence of the shoulders mentioned above, the result in Fig. 10 provides only a qualitative description of the generated wave profile.

D. Temporal multiple-shot collinear autocorrelation measurements

The third and last setup was realized with the aim of precisely monitoring the temporal profile at the central part of the WP by removing the contribution of lateral tails. To this end, we implemented a collinear autocorrelation scheme in which the central portion of the WP was selected by a suitable aperture placed as close as possible to the LBO output face. The data show the occurrence of pulse compression down to 20 fs at the beam center.

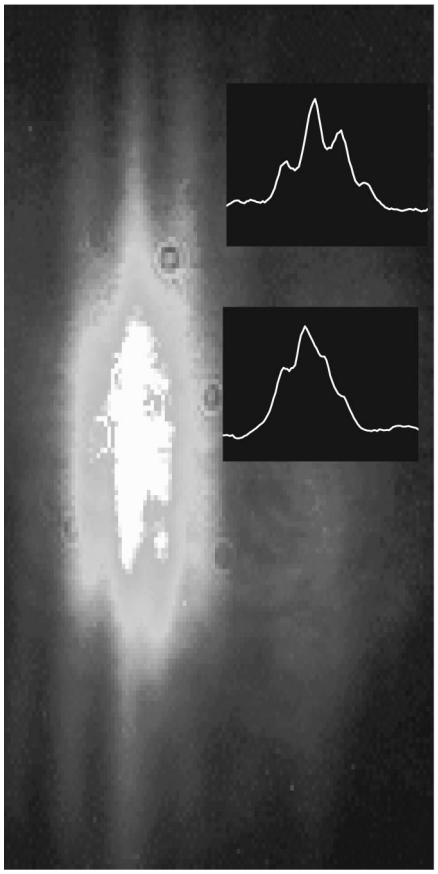

FIG. 10. Autocorrelation pattern in nonlinear regime (case II) of the FF pulse imaged from the output face of a 22-mm LBO crystal, and corresponding profiles (in white) at the top and center of the trace.

The experimental setup is schematized in Fig. 12. The collinear autocorrelation was performed by means of a standard scanning Michelson interferometer scheme, in type II phase-matching configuration with a 100-μm BBO crystal. A delay line with 11-fs step (double pass) was placed in one of the two arms. In order to get rid of the impact of the laser shot-to-shot fluctuations, a gated acquisition was implemented in which only a selected window of input pulse energies was accepted. The detection was realized by means of a silicon photodiode. As mentioned above, a 100-μm pinhole was placed at the output of the LBO (1 cm) for the selection of the central part of the WP. Measurements without pinhole were also performed for comparison. An f-2f-f imaging system (with magnification 1) was mounted, as for the case illustrated in Sec. II C, to prevent the effect of pulse broadening.

Results referring to the case-II focusing condition are presented in Fig. 13, where measurements with and without pinhole and a comparison with the linear case are shown.

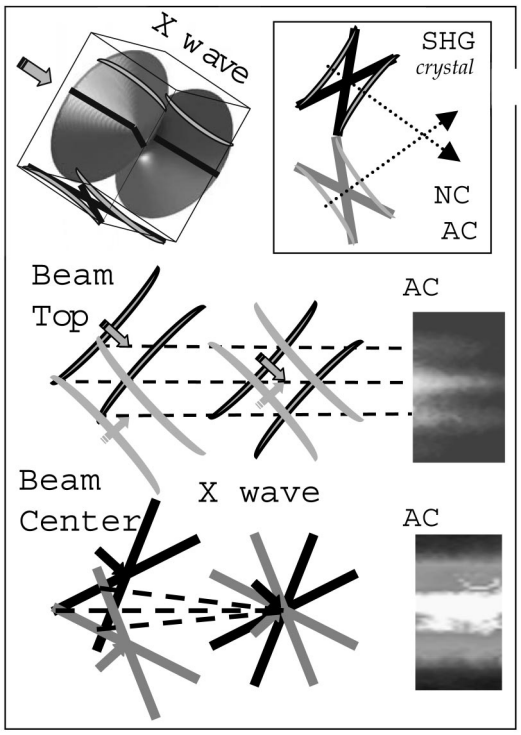

FIG. 11. Description of the collision of two ideal X waves inside the BBO crystal.

The estimated FWHM pulse duration measured with the aperture is 20 fs. This value is half the one obtained at $Z_{out} = 3.5$ cm with the single-shot noncollinear cross-correlation setup (see Fig. 7). The pulse broadening from 1 cm to 3.5 cm is consistent with the trend shown in Fig. 8(b). Note that, with the presence of the pinhole, the level of the shoulders was the smallest we have achieved. By removing the pinhole, the pulse broadens by two times and the shoulders level

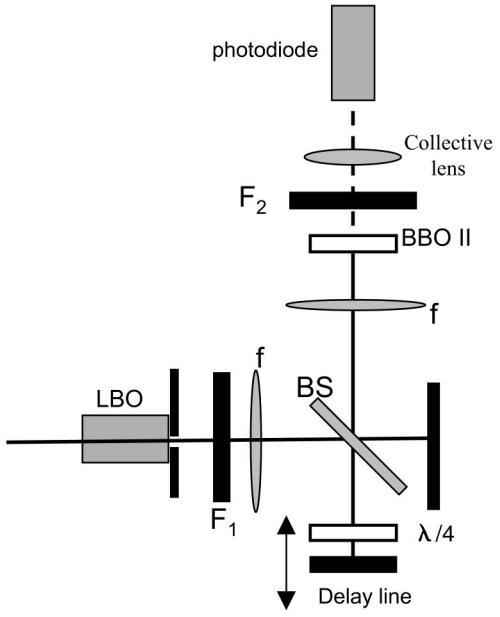

FIG. 12. Experimental setup for temporal multiple-shot autocorrelation measurements.

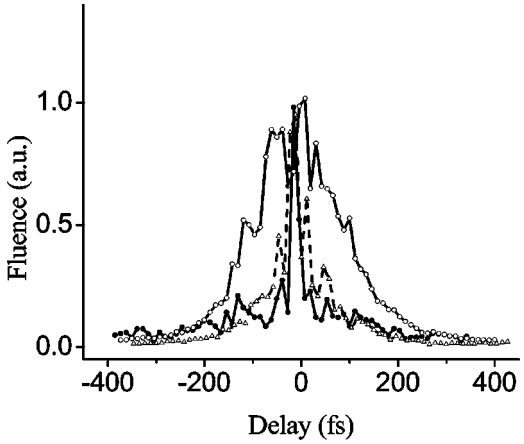

FIG. 13. Autocorrelation traces obtained in linear (white dots) and nonlinear (white triangles) regimes for collinear multiple-shots autocorrelation measurements without pinhole, and autocorrelation trace obtained in nonlinear regime with the pinhole (black dots). All curves are normalized to arbitrary units.

increases, due to the contribution of the WP tails. Note also that all traces are affected by oscillations that we interpret as due to the aliasing between the sampling frequency (11 fs) and the interferometric frequency (about 3 fs). We mention that interference effects might occur in this type II phase-matching configuration because of the transverse phase modulation of the FF and thus of the generated SF field.

In commenting on the data, we should say that the achieved 20 fs duration at the crystal output is a very remarkable result: if the huge value of the GVM between the FF and SH waves is considered, the occurrence of such a dramatic compression, in the presence of spatial trapping, necessarily implies the occurrence of a strong reshaping from Gaussian to X-type wave. Our numerical calculations (data not shown) indicate that also the cubic nonlinearity contributes in achieving a so relevant compression. In fact, while the pure quadratic model leads to a pulse duration of ~ 50 fs at the output, the model that takes into account the Kerr contribution provides a perfect quantitative agreement with the experimental result. However, the inclusion of the Kerr effect does not change qualitatively the process, leading only to a stronger compression and to a somewhat faster dynamics. In the experiments, as already mentioned in Sec. II A, we have noticed that a Kerr-driven type of collapse, accompanied by continuum generation, takes place at fairly higher pumping or for sharper focusing conditions. All the measurements reported in this paper refer to operating conditions in which the Kerr effect contributes only as a perturbation, the dynamics being strictly ruled by the saturable feature of the quadratic nonlinearity.

III. DISCUSSION AND CONCLUSIONS

In this paper, we have presented a detailed description of the experiments that have demonstrated the occurrence of spatiotemporal compression and quasistationary propagation sustained by $\chi^{(2)}$ nonlinear interaction in a 22-mm LBO crystal. In the regime of SHG with conventional Gaussian input pulses, spatial beam profiles measurements have shown

that diffraction has been virtually removed leading to the occurrence of 3D self-trapping between the FF and the generated SH envelopes; in case of positive phase-mismatch, normal GVD and large GVM. By combining the results obtained by noncollinear cross-correlation, noncollinear autocorrelation, and collinear autocorrelation, we have demonstrated that the beam focusing occurs together with a relevant pulse compression (from 170 fs to 20 fs) over the central part of the beam, while pulse splitting occurs along the (spatially) outer part of the beam. The free-space propagation of the generated FF WP features sub-Gaussian diffraction with a divergence 3–4 times smaller than what was expected for an equivalent Gaussian beam, by a 7 times temporal broadening over 10 cm, by a Bessel-type contribution (evidenced in the far field), and by angular dispersion. We mention that, in addition to what we have presented in this paper, we have recently developed a precise, three-dimensional mapping technique, and that we have successfully used it for the monitoring of the spatio-temporal profile of the generated WP. The experiment, which is based on the use of an ultrafast (20 fs) nonlinear gate and has been performed with a different laser system, different pulse duration and different setup, will be presented in detail elsewhere [68]. Here, we just mention that the results are fully consistent with what has been described here, showing very clearly the conical structure of the generated WP.

The resulting scenario is not understandable and not describable by treating space and time separately. In the latter framework, in fact, the observed spatiotemporal compression would be counterintuitive under our operating conditions. Indeed, in such a case, spatiotemporal self-focusing would require self-focusing nonlinearity and anomalous (negative) GVD. Vice versa, the positive GVD and very large GVM (our output 20 fs FF and SH Gaussian pulses would split in less than half millimeter in the absence of interaction) of our operating regime would lead to temporal broadening of the WPs at FF and SH, if a pure temporal dynamics would be considered. Therefore, if the spatial and temporal dynamics occur independently, we should not expect any localization. In fact, the temporal broadening should quench the spatial trapping because of the intensity reduction and the splitting between the FF and SH components, as it has been numerically predicted in planar waveguides (1+1+1D) and close to phase matching [69].

Our results clearly show that a nontrivial process takes place, where the dependence on the spatial and temporal degrees of freedom is not factorizable. The WP undergoes a dramatic reshaping during the nonlinear interaction leading to the spontaneous appearance of an X-type profile at the LBO crystal output, featured by temporal splitting only in the outer part of the beam. The observed spatial and temporal dynamics are a manifestation of this underlying phenomenon. The X-type nature of the WP is confirmed not only by the space-resolved correlation measurements but also by the analysis of the free-space propagation. In fact, the observed sub-Gaussian diffraction, temporal broadening, and angular dispersion are typical features of X-type waves [70]. The resulting scenario demonstrates how the spatiotemporal degree of freedom, that is the angular dispersion, and the nonlinearity, which couples modes at different angles and frequencies, forces the spontaneous reshaping of the WP in such a way that a localized state appears, under conditions for which a conventional separable WP would spread. To this end, we mention that, as already shown for linear X waves and for tilted pulses in $\chi^{(2)}$, the effective negative GVD caused by the angular dispersion can easily overcome the material chromatic dispersion, thus ruling the nonlinear dynamics. Different from previous works, here for the first time, to the best of our knowledge, the angular dispersion is not present in the input WP, but appears spontaneously as the consequence of the combined action of nonlinearity, diffraction, and dispersion.

The spontaneous appearance of X-shaped waves provides a strong indication of the existence of a new class of nonlinear localized stationary modes, for which mutual balance of phase modulation caused by diffraction, chromatic dispersion, and angular dispersion, respectively, can take place. Exact solutions of this kind exist, both for $\chi^{(2)}$ and for Kerr nonlinearities [62]. So far, the theoretical results show that these solutions have infinite energy as a consequence of their Bessel-like slow decay. Because of that, only approximate observation of these nonlinear X waves is accessible in real experimental settings. The key features of these WPs is the simultaneous presence of a high intensity central part where the nonlinearity plays the dominant role, and of weak but extended tails which undergo linear propagation. The nonlinear X waves, whose propagation features approach those of the linear regime, can be considered therefore as a new class of solitary waves living in the intermediate realm between the linear and the nonlinear world.

ACKNOWLEDGMENTS

The authors acknowledge the support of MIUR (Projects Nos. PRIN01 and FIRB01), UNESCO UVO-ROSTE (Contract No. 875.586.2), EC CEBIOLA (Contract No. ICA1-CT-2000-70027), and DGI BFM2002-04369-C04-03 (Spain). J.T. acknowledges the support of a postdoctoral grant from Ministerio de Educacion Cultura y Deporte (Spain). S.T. acknowledges discussions with R. Grunwald, and P.D.T. is thankful to G. Coppo and D. Caironi for their suggestions.

[1] G.I. Stegeman, D.J. Hagan, and L. Torner, Opt. Quantum Electron. **28**, 1691 (1996).

[2] K. Blow and G.I. Stegeman, J. Opt. Soc. Am. B **14**, 2950 (1997).

[3] L. Torner, in *Beam Shaping and Control with Nonlinear Optics*, edited by F. Kajzar and R. Reinisch (Plenum Press, New York, 1998).

[4] G. Stenmayer, D.H. Sutter, L. Gallmann, N. Matuschek, and U. Keller, Science **286**, 1507 (1999).

[5] R.Y. Chiao, E. Garmine, and H.C. Townes, Phys. Rev. Lett. **13**,

479 (1964).
[6] Y.R. Shen, *The Principles of Nonlinear Optics* (Wiley, New York, 1984).
[7] *Spatial Solitons*, edited by S. Trillo and W.E. Toruellas (Springer, Berlin, 2001).
[8] G.P. Agrawal, *Nonlinear Fiber Optics* (Academic Press, New York, 1995).
[9] D. Schumacher, Opt. Lett. **27**, 451 (2002).
[10] P.B. Corkum and C. Rolland, IEEE J. Quantum Electron. **25**, 2634 (1989).
[11] P.B. Corkum, C. Rolland, and T. Srinivasan-Rao, Phys. Rev. Lett. **57**, 2268 (1986).
[12] R. Loudon, *The Quantum Theory of Light*, 3rd ed. (Clarendon University Press, Oxford, 2000).
[13] A.T. Ryan and G.P. Agrawal, Opt. Lett. **20**, 306 (1995).
[14] J. Ranka and A. Gaeta, Opt. Lett. **23**, 534 (1998).
[15] P. Di Trapani, D. Caironi, G. Valiulis, A. Dubietis, R. Danielius, and A. Piskarskas, Phys. Rev. Lett. **81**, 570 (1998).
[16] E.J. Fonseca, S.B. Cavalcanti, and J.M. Hickmann, Opt. Commun. **169**, 199 (1999).
[17] A. Zozulya, S.A. Diddams, A.G. Van Engen, and T.S. Clement, Phys. Rev. Lett. **82**, 1430 (1999).
[18] F. Wise and P. Di Trapani, Opt. Photonics News **13**, 28 (2002).
[19] ''Light bullets'' denote spatiotemporal solitons self-trapped in 3D (x,y,t if z denotes the propagation direction in a bulk medium), as introduced by Y. Silberberg, Opt. Lett. **15**, 1282 (1990). Trapped states of this kind, however, were known long before in plasma, see J.I. Gersten and N. Tzoar, Phys. Rev. Lett. **35**, 934 (1975); C.J. McKinstrie and D.A. Russell, *ibid.* **61**, 2929 (1988). ''Bullets'' are used also to denote spatiotemporal trapping of waves of different origin, e.g., spin waves, M. Bauer, O. Buttner, S.O. Demokritov, B. Hillebrands, V. Grimalsky, Y. Rapoport, and A.N. Slavin, *ibid.* **81**, 3769 (1998).
[20] G. Valiulis, J. Kilius, O. Jedrkiewicz, A. Bramati, S. Minardi, C. Conti, S. Trillo, A. Piskarskas, and P. Di Trapani, in *OSA Trends in Optics and Photonics (TOPS)*, QELS 2001 Technical Digest, Vol. 57 (Optical Society of America, Washington D.C., 2001).
[21] J.N. Brittingham, J. Appl. Phys. **54**, 1179 (1983).
[22] R.W. Ziolkowski, Phys. Rev. **39**, 2005 (1989).
[23] J. Lu and J.F. Greenleaf, IEEE Trans. Ultrason. Ferroelectr. Freq. Control **39**, 19 (1992).
[24] H. Sönajalg and P. Saari, Opt. Lett. **21**, 1162 (1996).
[25] E. Recami, Physica A **252**, 586 (1998).
[26] J. Salo, J. Fagerholm, A.T. Friberg, and M.M. Salomaa, Phys. Rev. Lett. **83**, 1171 (1999).
[27] J. Salo, J. Fagerholm, A.T. Friberg, and M. Salomaa, Phys. Rev. E **62**, 4261 (2000).
[28] P. Saari, edited by O. Svelto *et al.*, *Ultrafast Processes in Spectroscopy* (Plenum Press, New York, 1996), p. 151.
[29] K. Reivelt and P. Saari, J. Opt. Soc. Am. A **17**, 1785 (2000).
[30] C.J.R. Sheppard, J. Opt. Soc. Am. A **18**, 2594 (2001).
[31] M.A. Porras, Opt. Lett. **26**, 1364 (2001).
[32] W. Hu and H. Guo, J. Opt. Soc. Am. B **19**, 49 (2002).
[33] S. Orlov, A. Piskarskas, and A. Stabinis, Opt. Lett. **27**, 2167 (2002).
[34] M.A. Porras, C. Conti, S. Trillo, and P. Di Trapani, Opt. Lett. (to be published).
[35] J. Durnin, J.J. Miceli, and J.H. Eberly, Phys. Rev. Lett. **58**, 1499 (1987).
[36] R.W. Ziolkowski, D.K. Lewis, and B.D. Cook, Phys. Rev. Lett. **62**, 147 (1989).
[37] J. Lu and J.F. Greenleaf, IEEE Trans. Ultrason. Ferroelectr. Freq. Control **39**, 441 (1992).
[38] H. Sönajalg, M. Rtsep, and P. Saari, Opt. Lett. **22**, 310 (1997).
[39] R. Grunwald, V. Kebbel, U. Griebner, U. Neumann, A. Kummrow, M. Rini, E.T.J. Nibbering, M. Piche, G. Rousseau, and M. Fortin (unpublished).
[40] P. Saari and K. Reivelt, Phys. Rev. Lett. **79**, 4135 (1997).
[41] Z. Jiang and X.C. Zhang, Opt. Express **5**, 243 (1999).
[42] D. Mugnai, A. Ranfagni, and R. Ruggeri, Phys. Rev. Lett. **84**, 4830 (2000).
[43] P. Saari, in *Times Arrows, Quantum Measurements, and Superluminal Behaviour*, edited by D. Mugnai (CNR, Rome, 2001).
[44] O.E. Martinez, IEEE J. Quantum Electron. **25**, 2464 (1989).
[45] G. Szabo and Zs. Bor, Appl. Phys. B: Photophys. Laser Chem. **50**, 51 (1990).
[46] O.E. Martinez, Opt. Commun. **59**, 229 (1986).
[47] S. Szatmari, P. Dimon, and M. Feuerhake, Opt. Lett. **21**, 1156 (1996).
[48] O.E. Martinez, J.P. Gordon, and R.L. Fork, J. Opt. Soc. Am. A **1**, 1003 (1984).
[49] O.E. Martinez, J. Opt. Soc. Am. B **3**, 929 (1986).
[50] M. Porras, G. Valiulis, and P. Di Trapani (unpublished); M. Porras, G. Valiulis, and P. Di Trapani (unpublished).
[51] P. Di Trapani, G. Valiulis, A. Piskarskas, O. Jedrkiewicz, J. Trull, C. Conti, and S. Trillo, arXiv:physics/0303083 (2003); Phys. Rev. Lett. (to be published).
[52] S. Trillo, C. Conti, P. Di Trapani, O. Jedrkiewicz, J. Trull, and G. Valiulis, in *Nonlinear Guided Waves and Their Application* (Optical Society of America, D.C. Washington, 2002), paper NLMB.
[53] A.V. Buryak, P. Di Trapani, D. Skryabin, and S. Trillo, Phys. Rep. **370**, 63 (2002).
[54] X. Liu, L.J. Qian, and F.W. Wise, Phys. Rev. Lett. **82**, 4631 (1999).
[55] X. Liu, K. Beckwitt, and F.W. Wise, Phys. Rev. Lett. **85**, 1871 (2000).
[56] S. Minardi, G. Blasi, P. Di Trapani, G. Valiulis, A. Berzanskis, A. Varanavicius, and A. Piskarskas (unpublished).
[57] S. Orlov, A. Piskarskas, and A. Stabinis, Opt. Lett. **27**, 2103 (2002).
[58] H.S. Eisenberg, R. Morandotti, Y. Silberberg, S. Bar-Ad, D. Ross, and V.S. Aitchison, Phys. Rev. Lett. **87**, 043902 (2001).
[59] J. Salo, J. Fagerholm, A.T. Friberg, and M.M. Salomaa, Phys. Rev. E **62**, 4261 (2000).
[60] G. Valiulis, A. Piskarskas, O. Jedrkiewicz, J. Trull, C. Conti, S. Trillo, and P. Di Trapani (unpublished); G. Valiulis, A. Piskarskas, P. Di Trapani, O. Jedrkiewicz, J. Trull, S. Trillo, and C. Conti (accepted for CLEO/EQEC, Munich, 2003).
[61] S. Trillo, C. Conti, P. Di Trapani, O. Jedrkiewicz, J. Trull, G. Valiulis, and G. Bellanca, Opt. Lett. **16**, 1451 (2002).
[62] C. Conti, S. Trillo, P. Di Trapani, G. Valiulis, A. Piskarskas, O. Jedrkiewicz, and J. Trull, Phys. Rev. Lett. **90**, 170406 (2003).
[63] P. Di Trapani, A. Bramati, S. Minardi, W. Chinaglia, C. Conti, S. Trillo, J. Kilius, and G. Valiulis, Phys. Rev. Lett. **87**, 183902 (2001).

[64] X. Liu, K. Beckwitt, and F. Wise, Phys. Rev. E **62**, 1328 (2000).
[65] W.E. Torruellas, Z. Wang, D.J. Hagan, E.W. Van Stryland, G.I. Stegeman, L. Torner, and C.R. Menyuk, Phys. Rev. Lett. **74**, 5036 (1995).
[66] R. Danielius, A. Stabinis, G. Valiulis, and A. Varanavicius, Opt. Commun. **105**, 67 (1994).
[67] Z. Sacks, G. Mourou, and R. Danielius, Opt. Lett. **26**, 462 (2001).
[68] J. Trull, O. Jedrkiewicz, P. Di Trapani, A. Matijosius, A. Varanavicius, G. Valiulis, R. Danielius, E. Kucinskas, A. Piskarskas, and S. Trillo (unpublished).
[69] S. Carrasco, J.P. Torres, D. Artigas, and L. Torner, Opt. Commun. **192**, 347 (2001).
[70] M. Porras, G. Valiulis, and P. Di Trapani (unpublished).